


Direct Observation of Enhanced Electron-Phonon Coupling in Copper Nanoparticles in the Warm-Dense Matter Regime

Quynh L. D. Nguyen^{1,*}, Jacopo Simoni,^{2,8} Kevin M. Dorney¹, Xun Shi,¹ Jennifer L. Ellis,¹ Nathan J. Brooks,¹ Daniel D. Hickstein³, Amanda G. Grennell,⁴ Sadegh Yazdi⁵, Eleanor E. B. Campbell^{6,7}, Liang Z. Tan⁸, David Prendergast⁸, Jerome Daligault,² Henry C. Kapteyn^{1,3} and Margaret M. Murnane¹

¹JILA, Department of Physics, University of Colorado and NIST, Boulder, Colorado 80309, USA
²Theoretical Division, Los Alamos National Laboratory, Los Alamos, New Mexico 87545, USA
³Kapteyn-Murnane Laboratories Inc., 4775 Walnut St #102, Boulder, Colorado 80301, USA
⁴Department of Chemistry, University of Colorado Boulder, Boulder, Colorado 80309 80309, USA
⁵Renewable and Sustainable Energy Institute, University of Colorado Boulder, Boulder, Colorado 80309, USA
⁶EaStCHEM, School of Chemistry, Edinburgh University, David Brewster Road, Edinburgh EH9 3FJ, United Kingdom
⁷Department of Physics, Ewha Womans University, Seoul 03760, Republic of Korea
⁸Molecular Foundry, Lawrence Berkeley National Laboratory, Berkeley, California 94720, USA

 (Received 20 December 2021; revised 27 June 2022; accepted 26 May 2023; published 21 August 2023)

Warm dense matter (WDM) represents a highly excited state that lies at the intersection of solids, plasmas, and liquids and that cannot be described by equilibrium theories. The transient nature of this state when created in a laboratory, as well as the difficulties in probing the strongly coupled interactions between the electrons and the ions, make it challenging to develop a complete understanding of matter in this regime. In this work, by exciting isolated ~ 8 nm copper nanoparticles with a femtosecond laser below the ablation threshold, we create uniformly excited WDM. Using photoelectron spectroscopy, we measure the instantaneous electron temperature and extract the electron-ion coupling of the nanoparticle as it undergoes a solid-to-WDM phase transition. By comparing with state-of-the-art theories, we confirm that the superheated nanoparticles lie at the boundary between hot solids and plasmas, with associated strong electron-ion coupling. This is evidenced both by a fast energy loss of electrons to ions, and a strong modulation of the electron temperature induced by strong acoustic breathing modes that change the nanoparticle volume. This work demonstrates a new route for experimental exploration of the exotic properties of WDM.

DOI: [10.1103/PhysRevLett.131.085101](https://doi.org/10.1103/PhysRevLett.131.085101)

Progress in several research areas depends on a detailed understanding of matter under extreme conditions of temperature and pressure. The “warm dense matter” (WDM) regime corresponds to matter with a density near those of solids and a temperature from ~ 10 to ~ 10000 K—a regime that cannot be described by equilibrium theories [1,2]. WDM lies at the heart of many interesting problems in high-energy density physics [3], fusion energy science [4], planetary science [5], and stellar astrophysics [6,7]. Enabled by advances in laser technology, the last decade has seen rapid progress in the ability to make and interrogate WDM in the laboratory [8–17]. However, despite these breakthroughs, it remains very challenging to accurately characterize the microscopic interactions within WDM, because of the transient nature of WDM creation in the lab, where dynamics can span from femtoseconds to much longer timescales. This makes it difficult to validate advanced theories.

Previous studies used high-power lasers, pulsed power, and ion beams at mid-scale and large-scale facilities to excite and probe WDM. These experiments have been

limited to relatively low repetition rates (< 120 Hz) [18] that influence what diagnostic measurements are possible. Additionally, the time resolution is often limited by the probing x-ray pulse duration or by streak camera diagnostics (> 2 ps) [19,20]. While ultrafast laser excitation at > 1 kHz repetition rates can enable faster and more accurate measurements, the short penetration depth of laser light into materials, exponentially decaying over ~ 10 nm [21], has represented a severe limitation to this approach. In a standard flat solid-target geometry, this means that the excitation and material phase of WDM change dramatically with depth [1,2,22]. Moreover, the high laser energy necessary to compress or superheat a sample typically causes irreversible damage, requiring a fresh sample for every laser shot [9,22]. X-ray heating of thin films can create a more-uniformly heated sample, but requires a large-scale free electron laser facility with limited repetition rate and access [10].

Here, we present a novel approach for overcoming these long-standing challenges. We uniformly heat isolated ~ 8 nm metallic nanoparticles (NPs) to just below the

ablation threshold using intense ~ 55 fs laser pulses. Because of their lower heat capacity, the electrons are preferentially heated by the laser to high temperatures, before losing energy to the ions (see Fig. 1). By using a time-delayed blue laser pulse to probe the hot electron Fermi distribution using photoelectron spectroscopy, we can directly measure the instantaneous electron temperature as a function of time (see Appendix A). This allows us to observe higher hot electron cooling rates and electron-phonon or ion coupling (G_{ei}) values than previously measured for bulk Cu. Then, by varying the excitation laser fluence, we can identify the melting threshold of the NPs, which is associated with very high electron-phonon or ion coupling. A comparison with theories of highly excited strongly interacting matter shows that the state of matter we produce lies at the boundary between hot solids and plasmas, where the electrons become strongly degenerate. This is evidenced by the high electron-phonon coupling, a strong modulation of the electron temperature by the breathing modes of the NP at later times, the existence of a threshold fluence associated with a change in electron-ion coupling, and the good comparison with theory. These results open a new avenue for experimental WDM research and can inform current and future theories.

We note that the isolated NP geometry has unique advantages compared with a flat target. In the NP, strong electron-phonon or ion coupling dominates over other mechanisms such as thermionic emission, or nanoplasma explosions that occur at higher laser fluences [26,27]. In the case of a flat target, plasma expansion or explosion and hot electron transport into the cooler substrate can also occur.

Hot electron temperature measurement and modeling of the electron-ion coupling.—By illuminating CuNPs with a moderately intense laser field (10^{12} W/cm²) below the ablation threshold, electrons are heated via inverse bremsstrahlung absorption. Very fast electron-electron scattering gives rise to a hot thermalized Fermi-Dirac distribution (within ~ 50 fs) [23–25] with a very high temperature of ~ 10000 K, that is initially much higher than that of the lattice [~ 1000 K, see Fig. 1(a)]. Next, scattering of hot

electrons with ions becomes the dominant relaxation mechanism, which leads to excitation of phonon modes on timescales >200 fs [23–25], followed by nonthermal melting of the lattice for sufficiently high laser fluences. After a few picoseconds, the ions and the electrons reach thermal equilibrium at temperatures ~ 3000 K. As the particle transforms from a solid to WDM, the lattice order vanishes and the electron charge density becomes more diffuse. Once the lattice exceeds the melting point of CuNPs ($T_{\text{melt}} = 1100$ K, see Supplemental Material, S1.3 [28]) beyond the threshold (melting) fluence $F_{\text{melt}} = 107$ mJ/cm², strong acoustic breathing modes are launched and modulate the volume of the CuNPs at ~ 3 ps and beyond [Fig. 2(c)]. Radiative cooling and evaporation of the superheated NP will then dominate after several hundred picoseconds.

First, to experimentally measure the instantaneous electron temperature (see Shi *et al.* [40]), we fitted the photoelectron energy distribution curves to a hot Fermi-Dirac distribution at different time delays after excitation [Figs. 2(a) and 2(b)]. We thus obtained the dynamical electron temperature (T_e) distributions for different laser fluences in the range 80–147 mJ/cm² [Fig. 2(c)].

Next, we used the following modified-two-temperature model (mod-TTM) to extract the electron-phonon coupling G_{ei} [Eqs. (1) and (2)] [41] for different laser fluences (F) (see Supplemental Material, S3-8 for further details). G_{ei} controls the energy transfer rate from the electrons to the phonons or ions.

$$C_e(T_e) \frac{\partial T_e}{\partial t} = \nabla(\gamma \nabla T_e) - G_{ei}(T_e - T_i) + \int dr \tilde{p}_e \nabla \cdot v + s S_{\text{laser}}(t), \quad (1)$$

$$C_i \frac{\partial T_i}{\partial t} = \nabla(\gamma \nabla T_i) + G_{ei}(T_e - T_i), \quad (2)$$

where C_e and C_i are the electron and ion heat capacities (see Supplemental Material, S5-7 [28]), T_e and T_i are the electron and ion temperatures, γ is the thermal conductivity,

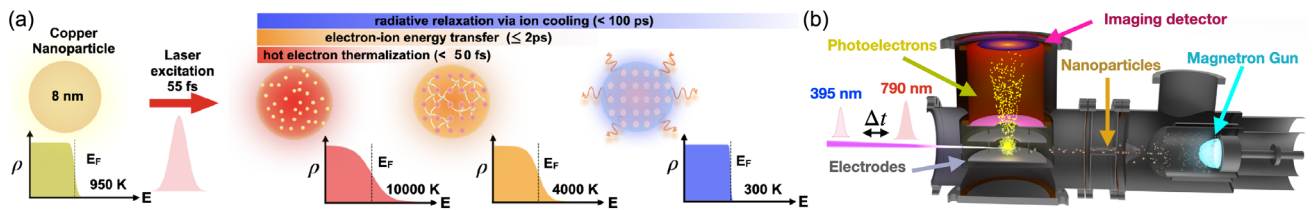


FIG. 1. Exciting and probing dynamics of warm dense Cu Nanoparticles (CuNPs). (a) After excitation by a 790-nm pulse, hot electrons thermalize on timescales <50 fs. This is followed by energy transfer from the electron bath to the lattice on timescales up to 2 ps [23–25]. The electron Fermi distribution (electron density ρ versus energy E) is shown, where E_F is the Fermi energy. (b) Experimental apparatus for *in vacuo* ultrafast photoelectron spectroscopy of CuNPs. A modified magnetron sputtering source produces monodisperse, highly pure CuNPs. Subsequently, they fly through a series of differential pumping stages and enter the interaction region where they interact with an infrared laser excitation pulse. A time-delayed blue probe pulse is then used to probe the hot electron distribution.

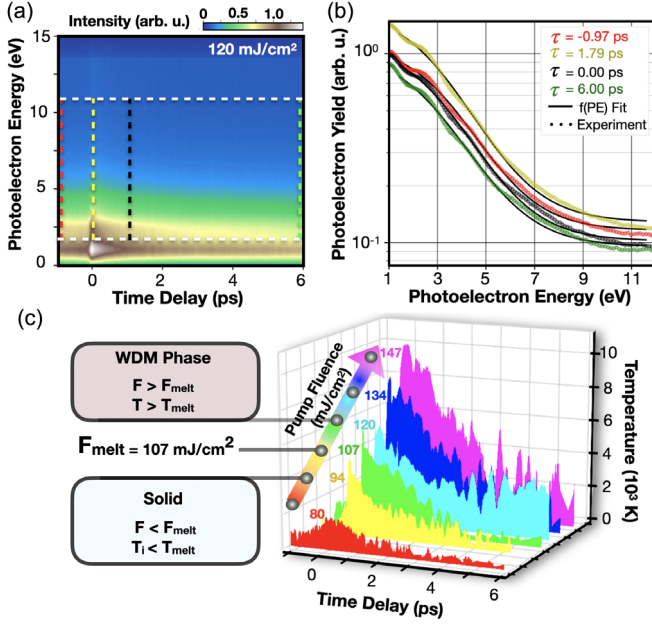


FIG. 2. Evolution of the hot electron temperature. (a) Photoelectron energy as a function of pump-probe delay for pump laser fluence of 120 mJ/cm². Dashed colored lines indicate the photoelectron spectra (PES) at different time delays. The horizontal dashed white lines indicate the energy range for the fitting. (b) PES at time delays that correspond to the colored-dashed lines in panel (a) on a semilog-scale. The solid black lines show numerical fits of the data to thermal distributions, which are used to extract the electron temperature at each time delay. (c) T_e profiles as a function of time delay for pump fluences around $F_{\text{melt}} = 107$ mJ/cm².

$S_{\text{laser}}(t)$ is the laser heat source, \tilde{p}_e is the effective electron pressure, $\nabla \cdot v$ is the divergence of the electron velocity, and s is the surface enhancement factor (see Supplemental Material, S3). As a first-order approximation, we assume that G_{ei} in Eq. (1) is constant over the time-delay range of our measurements (see Appendix B) and set the electron pressure term, $\int dr \tilde{p}_e \nabla \cdot v$ to zero, which is denoted as simple TTM. We made this assumption due to the extra degree of complexity from the system undergoing extreme changes, such as the oscillations of T_e , that renders the extraction of G_{ei} as a function of time unfeasible. We fit the simple TTM solution to the measured T_e by varying G_{ei} [see Supplemental Material, S8, Fig. 3(a)] for the first 3 ps, before the onset of acoustic oscillations [Fig. 2(c)]. We then repeat this procedure for all laser fluences. The extracted peak T_e with corresponding T_i from the simple TTM model for each measured T_e time profile at all laser fluences are shown in Fig. 3(b). We calculate G_{ei} using quantum molecular dynamics (QMD) using the fitted peak T_e and T_i [Fig. 3(b)], and compare theory to our measurements. The extracted and calculated G_{ei} are displayed as a function of peak T_e [Fig. 3(c)]. We then develop and model the oscillatory behavior using the additional electron pressure (or pressure-volume) term [Eq. (1), Fig. 3(d)].

As the solid-WDM phase transition occurs, the electrons become strongly degenerate, as more d electrons are excited and start participating in the electron-ion energy exchange, leading to an increase in G_{ei} [45]. Interestingly, we observe a stronger variation for G_{ei} than previously reported for ~ 70 -nm thick Cu foil [20,43,46,47], which plateaus at ~ 4 to 6×10^{17} W/Km³ from 10 000 to 18 000 K while our measured G_{ei} increases rapidly from $1.3 \pm 0.3 \times 10^{17}$ to $8.2 \pm 0.9 \times 10^{17}$ W/Km³ for $T_e \sim 1800$ to 6000 K, beyond which it plateaus [Fig. 3(c)]. Our measured G_{ei} are twice as high as those reported in prior works for flat-CuWDM, which used fluences that are 2 times higher. While these prior studies focus purely on the WDM regime, we vary the excitation laser fluence to observe variation in the properties of the CuNPs as they undergo a phase transformation from solid to WDM.

We compare our measurements with the theoretical models developed by Simoni *et al.* [42] for bulk WD plasmas. We numerically evaluated G_{ei} (see Supplemental Material, S8 [28]) using this approach with the electronic and ionic structures calculated with density functional theory (DFT) based QMD [42]. Both theoretical (green dashed line) and experimental G_{ei} increase at higher T_e ; however, the measured values increase more strongly with temperature [Fig. 3(c)]. Meanwhile, we also computed the temperature dependent G_{ei} using the model of Lin *et al.* [48,49]. In which, G_{ei} is expressed as the product of the coupling (G_{ei}^0) at room temperature and a correction factor that depends on the density of states (DOS) to account for the number of thermally excited electrons. The Simoni approach accurately reproduced our measured G_{ei} at $T_e \sim 1800$ K and the measured coupling for solid Cu [20,44] at room temperature, so-called G_{ei}^0 . We set G_{ei}^0 in the Lin model to this value, the so-called ‘‘Lin + Simoni’’ model (blue dashed-dot line), and obtained excellent agreement with our measurements [Fig. 3(c)].

For the case of WD nanoparticles, we note that additional relaxation mechanisms likely play a crucial role, that are not usually considered in existing models for flat-Cu [42,48–50]. These include excitation of volume-modulated phonon modes and quantum confinement effects for NPs. We observe a strong modulation that occurs after 3 ps at $F \geq F_{\text{melt}}$ that signals a phase transition. This is due to changes in the particle volume as the lattice order vanishes [12,14] that cause the electrons to be more diffuse as the particle melts (see Appendixes C and D, Supplemental Material [28], S11). The simple TTM model disagrees strongly with the measured T_e for $F > F_{\text{melt}}$ and $t > 3$ ps, which indicates that the volume-pressure effects become significant as the particle transforms from solid to WDM. Furthermore, our QMD calculations predict a prominent pressure increase (>150 kBar) associated with this phase change (see Appendix C).

To understand the influence of the volume variation on T_e , we introduce a pressure-volume term that accounts

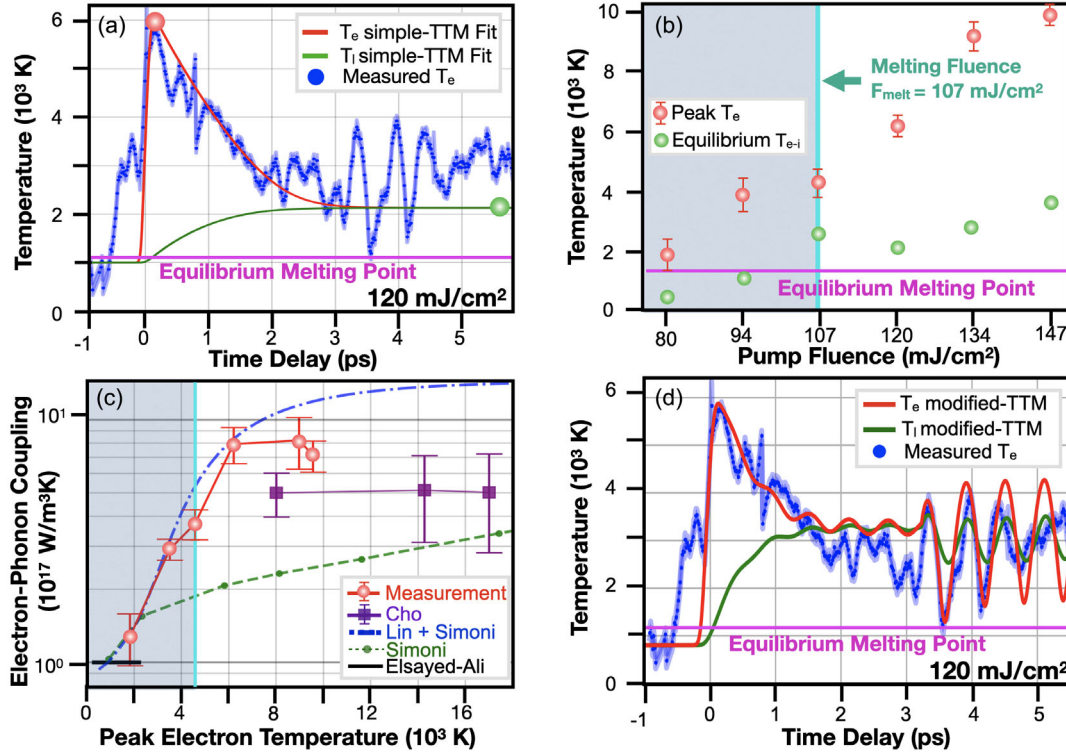


FIG. 3. Electron-ion (phonon) couplings in warm-dense CuNPs. (a) Simple-TTM (without pressure) fit applied to the T_e profile at 120 mJ/cm² to extract G_{ei} . T_e (red) and T_i (green) are the fits obtained for the electron and ion temperature profiles, where the error bars for T_e are in shaded blue. The magenta solid line indicates the melting temperature for CuNPs, $T_{melt} = 1100$ K. The peak- T_e (red circle) and equilibrium electron-ion temperature T_{e-i} (green circle) are determined from the T_e and T_i fits. Note that the pump-probe delay time of 0 fs does not reflect the arrival time, which is closer to around -0.5 ps. This was done for the purposes of the curve fitting. (b) The extracted peak- T_e and T_{e-i} are shown for $F = 80$ to 147 mJ/cm², where the lattice temperature exceeds T_{melt} at $F_{melt} = 107$ mJ/cm². The solid and WDM regimes are separated by a turquoise vertical line, where the blue region represents $T_i < T_{melt}$ and white region shows $T_i > T_{melt}$. We use this same notation in panel (c). (c) G_{ei} fitted from the simple-TTM and displayed as a function of the peak- T_e corresponding to each fluence. Theoretical G_{ei} are calculated using Lin + Simoni (blue), and Simoni (green) models [42]. The measurements for flat-CuWDM (purple) [43] and solid Cu [44] (black) are included for comparison. (d) The obtained G_{ei} from simple-TTM and measured phonon mode (1.9 THz) are implemented into the modified-TTM for the same data shown in panel (a). T_e (red) and T_i (green) profiles are predicted using the semi-empirical modified-TTM. The error bars in all panels indicate 95% confidence interval.

for the energy change due to modulation in the volume of the NP, $\int dr \tilde{p}_e \nabla \cdot v$ [Eqs. (1) and (2), see Appendixes C and D, Supplemental Material [28], S11, and Figs. 3(c) and 3(d)]. We performed a Fourier transform of the T_e and determined that the frequency of the large modulation is 1.9 THz, which is also in agreement with our MD simulations (see Supplemental Material, S10 [28]). We note that similar oscillations have recently been observed in 2D materials at high laser fluences, where T_e is modulated by coherent phonons associated with a charge density wave distortion [51]. Both represent evidence for strong electron-phonon or electron-ion couplings. These surprising phenomena that we observed experimentally may be uniquely associated with the intrinsic properties of isolated NPs, where hot electrons are confined more effectively than in a flat-target geometry, and thus have not been previously reported [12,20,43,46].

Electron-ion coupling dynamics.—We applied a phenomenological exponential model convoluted with the

instrument response function (IRF) to further understand coupling to the ions as well as radiation or evaporation loss (see Supplemental Material, S12). To directly compare the electron-ion energy transfer rate (k_{ei}) of CuNPs as the particle crosses the solid-WDM phase transition, we compare the measured T_e profiles and cooling rates for fluences below (94 mJ/cm²) and above (120 mJ/cm²) F_{melt} at 107 mJ/cm² [Figs. 4(a) and 4(b)]. The fitted $1/e$ time constants ($\tau_{ei} = 1/k_{ei}$) for the temperature profiles in the solid and WDM regimes are shown in Fig. 4(c). The phase transformation leads to modifications in the electron-DOS and the heat capacity that influence k_{ei} . At higher T_e , the temperature dependence of C_e reduces k_{ei} [52] while G_{ei} exhibits an opposite effect. Within the solid and WDM regimes, τ_{ei} increases with higher T_e , which indicates that the influence of C_e dominates over G_{ei} [Fig. 4(c)]. However, C_e drops at the solid-WDM boundary, F_{melt} , and enhances k_{ei} . As a result, τ_{ei} exhibits a sudden drop, or a kink, at F_{melt} that signals the phase

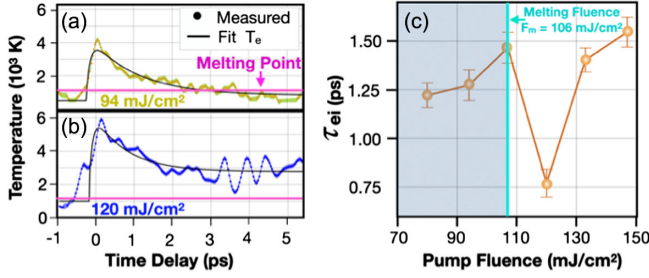


FIG. 4. Hot electron dynamics of CuNPs. Extracted temporal evolution of T_e at pump fluences of (a) 94 mJ/cm^2 (below F_{melt}) and (b) 120 mJ/cm^2 (above F_{melt}) to compare the volume-surface effects for CuNPs crossing the phase transition temperature. The solid black lines represent a fit to the data convoluted with the IRF of 99 ± 1 fs (see Supplemental Material, S12), and are used to determine τ_{ei} . The magenta solid horizontal line indicates T_{melt} for CuNPs. (c) Extracted τ_{ei} for all pump fluences with error bars within 95% confidence intervals. The turquoise vertical line indicates F_{melt} at 107 mJ/cm^2 .

transition. Our extracted τ_{ei} for the WD-nanomatter at $T_e \sim 10\,000$ K (1.5 ± 0.1 ps) is ~ 1.3 ps shorter than that reported for flat-Cu WDM (2.8 ± 0.4 ps) [43]. This is likely due to the additional thermalization mechanisms occurring in the WD nanomatter. For example, the pressure change connected to the time variation in the NP volume can speed up energy redistribution in the superheated CuNPs. This effect has also been theoretically predicted to accelerate the electron-ion heat exchange process in WD plasmas [53,54] and observed for semiconductors and semimetals [55–57].

In conclusion, we have developed a novel method for probing the strong electron-ion coupling that is present in uniformly excited WDM—in this case laser-excited Cu NPs. By tracking the instantaneous hot electron temperature for different pump fluences as a function of time, we can precisely extract the G_{ei} as the NPs undergo a phase transformation to WDM. The measured G_{ei} attains a maximal value of $(8.2 \pm 0.9) \times 10^{17} \text{ W/Km}^3$ over the transient electron temperature range from 1800 to 10 000 K, which is higher than previously measured for bulk Cu. Additionally, we experimentally and theoretically observe a large modulation on picosecond timescales in T_e when the particle melts, as a result of the dramatic increase in the pressure accompanying a solid-to-WDM transformation. This study introduces a generalizable approach to the study of WDM phenomena across a wide range of different materials via the use of isolated nanoparticles. Finally, our direct measurements of electron energy loss can validate advanced theories that can include effects of particle size, laser excitation parameters, pressure change, and strongly coupled phonon modes on the electron-ion coupling and cooling pathways.

This work was supported by the DOE Office of Basic Energy Sciences Award No. DE-FG02-99ER14982.

Q. L. D. N., J. L. E., N. J. B., and A. N. G. were also supported by the National Science Foundation Graduate Research Fellowship (DGE–1144083). S. Y. acknowledges support from the Facility for Electron Microscopy of Materials at CU Boulder (CU FEMM, RRID: SCR_019306). E. E. B. C acknowledges support of a JILA visiting fellowship. J. S. and J. D. were supported by the Laboratory Directed Research and Development program of Los Alamos National Laboratory under Project No. 20200074ER. Theoretical modeling by J. S., L. Z. T., and D. P. was facilitated through a user project at the Molecular Foundry at Lawrence Berkeley National Laboratory, which is supported by the Office of Science, Office of Basic Energy Sciences, of the U.S. Department of Energy under Contract No. DE-AC02-05CH11231. Calculations were performed using resources of the National Energy Research Scientific Computing Center (NERSC), a U.S. Department of Energy Office of Science User Facility located at Lawrence Berkeley National Laboratory, operated under Contract No. DE-AC02-05CH11231.

Appendix A: Methods.—We use a magnetron sputtering source to produce a continuous flow of ligand-free, isolated NPs in the gas phase (Fig. 1, see Supplemental Material, S1.1 [28]), allowing for kHz repetition-rate data acquisition. The measured temperature before laser excitation is ~ 1000 K (extracted in a similar fashion to Shi *et al.* [40]); thus, the NPs start as conventional hot NPs. We characterized their size and shape using aberration-corrected scanning transmission electron microscopy (AC-STEM). The source yields fresh NPs that are uniform in size and shape [58] for every laser shot, circumventing any issues due to sample degradation by the excitation laser. Most importantly, the size of the NP (8.2 ± 1.1 nm, see Supplemental Material, S1.2 [28]) is smaller than the absorption depth (~ 13 nm) at the excitation wavelength of 790 nm (1.5 eV photon energy), enabling homogenous heating and rapid thermalization of the electrons to a hot Fermi-Dirac distribution throughout the sample, and a near-complete elimination of effects due to spatial diffusion of heat at later times [Fig. 1(a)]. The NP is first excited with an intense 790-nm pulse to excite electrons above the Fermi level, and then probed using a 395-nm pulse to ionize the atoms and capture the resulting electron (and phonon) dynamics (see Supplemental Material, S2 [28]). We use laser intensities below the explosion threshold [26,27] to uniformly heat the NP. After ionization, the photoelectrons are guided to an imaging detector.

Appendix B: Fitting & modeling of G_{ei} with simple-TTM.—The experimental G_{ei} is extracted by fitting the $T_e(t)$ solution of the TTM set of equations with the experimentally extracted T_e profile. This requires a knowledge of the C_i that is kept constant at $3.5 \times 10^6 \text{ J/Km}^3$, in agreement with the Dulong-Petit law [44].

The C_e of Fig. S6 [28] is used in the TTM equations to account for the time variation in C_e (which is implicit in its temperature dependence). We have also incorporated the field enhancement (s) at the surface of the NP, which is numerically obtained using finite element modeling. We neglect the spatial diffusion contribution $\nabla(\gamma\nabla T_e)$ in Eq. (1) as a result of homogenous heating of the NP. The extraction of G_{ei} from the measured T_e profiles are shown in Supplemental Material, S8 [28].

Appendix C: Origin of pressure-volume contribution to the modified-TTM.—Figures 2(c), 3(a), and 3(c) show that strong oscillations in amplitude appear at 3 ps due to a significant volume change as the solid-liquid-WDM transition occurs. This is also how long it takes the electron and ion bath to equilibrate. Such modulation corresponds to an isotropic expansion and contraction of the NP. To understand this phenomenon, we model the dynamics of the NPs through the following set of hydrodynamical equations

$$\frac{dn_e(t)}{dt} = -n_e \vec{\nabla} \cdot \vec{v}, \quad (\text{C1})$$

$$n_e \frac{du_e(t)}{dt} = \vec{\nabla} \cdot \vec{q}_e - p_e \vec{\nabla} \cdot \vec{v} - \vec{\Pi} : \vec{\nabla} \vec{v} + Q_{ei}, \quad (\text{C2})$$

where \vec{v} is the electronic fluid velocity field, $\vec{\nabla} \cdot \vec{q}_e$ is the heat conduction, $p_e \vec{\nabla} \cdot \vec{v}$ is the work associated with the volume expansion and contraction, $\vec{\Pi} : \vec{\nabla} \vec{v}$ is the electronic viscosity of the NP due to heating, and Q_{ei} is the energy exchange between electrons and ions. We integrate Eq. (C2) over the NP volume to obtain Eq. (1), where $\tilde{p}_e = p_e + (\partial u_e / \partial v_e)_{T_e}$. We solve the equation of motion for compressible liquid NPs by neglecting the heat conduction term due to uniform heating and assuming that \vec{v} is driven by a single “breathing” mode and obtain the following expression for the pressure-volume (P-V) term

$$\left[\int_0^1 dx x^2 \tilde{p}_e(xR_t) (\partial_x U(x) + \frac{2}{x} U(x)) \right] \frac{dV_t}{dt}, \quad (\text{C3})$$

where $V_t = (4\pi/3)R_t^3$ and $U(x) = (d/dx)[\sin(x)/x]$, and the radius of the NP varies dynamically at the measured acoustic phonon “breathing” frequency (see Supplemental Material, Fig. S8 [28]). The solution of this modified-TTM model accounts for a significant pressure increase at the melting threshold as we calculated in Eq. (S2) [28].

Using QMD, we computed the electronic pressure of Cu at different conditions of temperature and density. We compare the pressure of solid Cu with the pressure obtained for liquid and disordered copper at higher temperatures (Fig. 5). The distinct difference between the pressure of solid and liquid Cu determines that the transition from solid

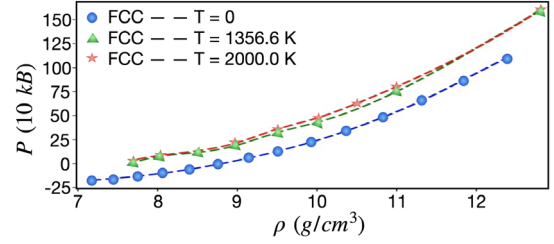


FIG. 5. Cu electronic pressure. The calculated electronic pressures for zero temperature solid FCC Cu (blue), liquid Cu at $T_{\text{melt}} = 1356$ K (green) and 2000 K (red) at varying densities.

to WDM leads to a dramatic increase in pressure of the NPs.

Appendix D: Temperature variation and time variation of surface electron density.—The isotropic expansion and contraction of the NPs is coherent as we observe this phenomenon in both solid and liquid CuNPs (Fig. 6). There may be some liquidlike instability, but this is not the primary driver of this large oscillation. We observe a softening of the acoustic phonon mode from 1.9 to 1.6 THz after 3 ps. This is due to the volume expansion of the NP and results in the phonon mode to oscillate at a slower frequency. We expect amplitude to be inversely proportional to the frequency of the phonon mode. As the NP expands, the frequency of oscillation softens and causes the amplitude of the oscillation to enhance.

To understand the dynamics and temperature dependence of the electronic distribution close to the surface of the NPs, we simulated the surface by modeling it with a slab of Cu atoms using DFT. We impose periodic boundary

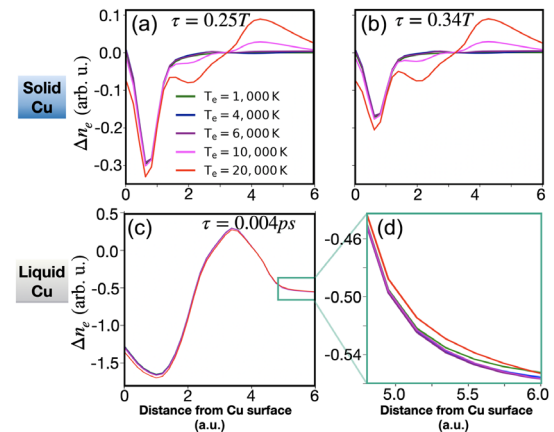


FIG. 6. Time- and temperature variation of the surface electron density for solid and liquid Cu NPs calculated using a slab model at (a) 0.2T and (b) 0.34T for solid, and at (c) 0.004 ps (zoom in (d)) for liquid Cu. T is the period of the acoustic phonon mode at 1.9 THz. The variation in the electron density at different times is due to fluctuations in the atomic positions. In both systems, the magnitude of the charge density migrates further away from the surface at higher electronic temperatures. Particularly in liquid, at higher electronic temperatures it increases in magnitude.

conditions in all three dimensions, and leave an empty space between two consecutive Cu slabs of approximately 7-atomic units (equivalent to 2/3 of the height of a supercell). We let the system evolve in time by moving the surface atoms according to an out-of-plane acoustic phonon mode that simulates the thermal expansion and contraction observed in the NP [Fig. 6(a)]. Hence, we computed the surface electron density, $n_e(r)$, of the copper slab along this trajectory as a function of T_e from 1000–20 000 K (Fig. 6). The electron density along the out-of-plane direction can be expressed as

$$n_e(z) = \iint_{\text{surface}} dx dy n_e(r). \quad (\text{D1})$$

To compare the dynamical charge fluctuation between solid and liquid Cu as a function of temperature, we employ QMD to simulate the NP surface with a 32 atoms slab at melting temperature under similar periodic boundary conditions as described for the solid Cu slab. For both solid and liquid Cu, we observe a variation in the electron density over time due to the dynamics of the atoms. The electron population also migrates further away from the surface as the temperature increases (Fig. 6). These calculations indicate a more pronounced variation of the liquid or WDM state charge density with respect to the solid case due to stronger fluctuations in the atomic positions with a consequent stronger modulation of the electronic DOS.

*Quynh.L.Nguyen@colorado.edu

Present address: Stanford PULSE Institute and Linac Coherent Light Source, SLAC National Accelerator Laboratory and Stanford University, Menlo Park, California 94025, USA.

- [1] At the Frontier of Scientific Discovery, U.S. DOE Report of the Panel on Frontiers of Plasma Science, 2017, https://science.osti.gov/-/media/fes/pdf/program-news/Frontiers_of_Plasma_Science_Final_Report.pdf.
- [2] R. W. Lee *et al.*, Finite temperature dense matter studies on next-generation light sources, *J. Opt. Soc. Am. B* **20**, 770 (2003).
- [3] S. Lebedev, *High Energy Density Laboratory Astrophysics* (Springer, New York, 2007).
- [4] S. H. Glenzer *et al.*, Symmetric inertial confinement fusion implosions at ultra-high laser energies, *Science* **327**, 1228 (2010).
- [5] J. H. Nguyen and N. C. Holmes, Melting of iron at the physical conditions of the Earth's core, *Nature (London)* **427**, 339 (2004).
- [6] T. Guillot, Interiors of giant planets inside and outside the solar system, *Science* **286**, 72 (1999).
- [7] R. A. Heinonen, D. Saumon, J. Daligault, C. E. Starrett, S. D. Baalrud, and G. Fontaine, Diffusion coefficients in the envelopes of white dwarfs, *Astrophys. J.* **896**, 2 (2020).
- [8] R. Ernstorfer, M. Harb, C. T. Hebeisen, G. Sciaini, T. Dartigalongue, and R. J. Dwayne Miller, The formation of warm dense matter: Experimental evidence for electronic bond hardening in gold, *Science* **323**, 1033 (2009).
- [9] B. Nagler, Turning solid aluminium transparent by intense soft x-ray photoionization, *Nat. Phys.* **5**, 693 (2009).
- [10] S. M. Vinko *et al.*, Creation and diagnosis of a solid-density plasma with an x-ray free-electron laser, *Nature (London)* **482**, 59 (2012).
- [11] R. R. Fäustline *et al.*, Observation of Ultrafast Nonequilibrium Collective Dynamics in Warm Dense Hydrogen, *Phys. Rev. Lett.* **104**, 125002 (2010).
- [12] B. Mahieu, N. Jourdain, K. Ta Phuoc, F. Dorchies, J.-P. Goddet, A. Lifschitz, P. Renaudin, and L. Lecherbourg, Probing warm dense matter using femtosecond x-ray absorption spectroscopy with a laser-produced betatron source, *Nat. Commun.* **9**, 3276 (2018).
- [13] K. Falk, Experimental methods for warm dense matter research, *High Power Laser Sci. Eng.* **6**, e59 (2018).
- [14] L. B. Fletcher *et al.*, Ultrabright x-ray laser scattering for dynamic warm dense matter physics, *Nat. Photonics* **9**, 274 (2015).
- [15] A. C. Hayes *et al.*, Plasma stopping-power measurements reveal transition from non-degenerate to degenerate plasmas, *Nat. Phys.* **16**, 432 (2020).
- [16] A. B. Zylstra *et al.*, Measurement of Charged-Particle Stopping in Warm Dense Matter, *Phys. Rev. Lett.* **114**, 215002 (2015).
- [17] *Frontiers and Challenges in Warm Dense Matter*, edited by F. Graziani *et al.* (Springer-Verlag, Heidelberg, 2014).
- [18] S. H. Glenzer *et al.*, Matter under extreme conditions experiments at the Linac Coherent Light Source, *J. Phys. B* **49**, 092001 (2016).
- [19] J. Feng, K. Engelhorn, B. I. Cho, H. J. Lee, M. Greaves, C. P. Weber, R. W. Falcone, H. A. Padmore, and P. A. Heimann, A grazing incidence x-ray streak camera for ultrafast, single-shot measurements, *Appl. Phys. Lett.* **96**, 134102 (2010).
- [20] B. I. Cho *et al.*, Electronic Structure of Warm Dense Copper Studied by Ultrafast X-ray Absorption Spectroscopy, *Phys. Rev. Lett.* **106**, 167601 (2011).
- [21] P. B. Johnson and R. W. Christy, Optical constants of the noble metals, *Phys. Rev. B* **6**, 4370 (1972).
- [22] F. Dorchies *et al.*, Unraveling the Solid-Liquid-Vapor Phase Transition Dynamics at the Atomic Level with Ultrafast X-Ray Absorption Near-Edge Spectroscopy, *Phys. Rev. Lett.* **107**, 245006 (2011).
- [23] J.-Y. Bigot, V. Halté, J.-C. Merle, and A. Daunois, Electron dynamics in metallic nanoparticles, *Chem. Phys.* **251**, 181 (2000).
- [24] J. G. Fujimoto, J. M. Liu, E. P. Ippen, and N. Bloembergen, Femtosecond Laser Interaction with Metallic Tungsten and Nonequilibrium Electron and Lattice Temperatures, *Phys. Rev. Lett.* **53**, 1837 (1984).
- [25] R. W. Schoenlein, W. Z. Lin, J. G. Fujimoto, and G. L. Eesley, Femtosecond Studies of Nonequilibrium Electronic Processes in Metals, *Phys. Rev. Lett.* **58**, 1680 (1987).
- [26] D. D. Hickstein *et al.*, Observation and Control of Shock Waves in Individual Nanoplasmas, *Phys. Rev. Lett.* **112**, 115004 (2014).

- [27] D. D. Hickstein *et al.*, Mapping Nanoscale absorption of femtosecond laser pulses using plasma explosion imaging, *ACS Nano* **8**, 8810 (2014).
- [28] See Supplemental Material at <http://link.aps.org/supplemental/10.1103/PhysRevLett.131.085101> for extended discussions on the methods, analysis, and modeling, which includes Refs. [29–39].
- [29] H. Haberland, M. Mall, M. Moseler, Y. Qiang, T. Reiners, and Y. Thurner, Filling of micron-sized contact holes with copper by energetic cluster impact, *J. Vac. Sci. Technol. A* **12**, 2925 (1994).
- [30] C. Chen, Z. Hu, Y. Li, L. Liu, H. Mori, and Z. Wang, In-situ high-resolution transmission electron microscopy investigation of overheating of Cu nanoparticles, *Sci. Rep.* **6**, 19545 (2016).
- [31] A. T. Eppink and D. H. Parker, Velocity map imaging of ions and electrons using electrostatic lenses: Application in photoelectron and photofragment ion imaging of molecular oxygen, *Rev. Sci. Instrum.* **68**, 3477 (1997).
- [32] D. H. Parker and A. T. Eppink, Photoelectron and photofragment velocity map imaging of state-selected molecular oxygen dissociation/ionization dynamics, *J. Chem. Phys.* **107**, 2357 (1997).
- [33] C. Multiphysics, Introduction to COMSOL Multiphysics. Extregistered, *COMSOL Multiphysics* (Burlington, MA, 1998), accessed 9 February 2018.
- [34] E. W. Hanse and P.-L. Law, Recursive methods for computing the Abel transform and its inverse, *J. Opt. Soc. Am. A* **2**, 510 (1985).
- [35] E. W. Hansen, Fast Hankel transform algorithm, *IEEE Trans. Acoust. Speech Signal Proc.* **33**, 666 (1985).
- [36] C. C. Blackstone, Photoelectron angular distributions in detachment from polarized d-like states: The case of HO₂, *Mol. Phys.* **119**, e1831636 (2020).
- [37] P. Giannozzi *et al.*, QUANTUM ESPRESSO: A modular and open-source software project for quantum simulations of materials, *J. Phys. Condens. Matter* **21**, 395502 (2009).
- [38] P. Giannozzi *et al.*, Advanced capabilities for materials modeling with quantum ESPRESSO, *J. Phys. Condens. Matter* **29**, 465901 (2017).
- [39] I. T. Todorov, W. Smith, K. Trachenko, and M. T. Dove, DL_POLY_3: New dimensions in molecular dynamics simulations via massive parallelism, *J. Mater. Chem.* **16**, 1911 (2006).
- [40] X. Shi *et al.*, Ultrafast electron calorimetry uncovers a new long-lived metastable state in 1T-TaSe₂ mediated by mode-selective electron-phonon coupling, *Sci. Adv.* **5**, eaav4449 (2019).
- [41] S. I. Anisimov *et al.*, Electron emission from metal surfaces exposed to ultrashort laser pulses, *Zh. Eksp. Teor. Fiz.* **66**, 375 (1974), http://www.jetp.ras.ru/cgi-bin/dn/e_039_02_0375.pdf.
- [42] J. Simoni and J. Daligault, Calculation of electron-ion temperature equilibration rates and friction coefficients in plasmas and liquid metals using quantum molecular dynamics, *Phys. Rev. E* **101**, 013205 (2020).
- [43] B. I. Cho, T. Ogitsu, K. Engelhorn, A. A. Correa, Y. Ping, J. W. Lee, L. J. Bae, D. Prendergast, R. W. Falcone, and P. A. Heimann, Measurement of electron-ion relaxation in warm dense copper, *Sci. Rep.* **6**, 18843 (2016).
- [44] H. E. Elsayed-Ali, T. B. Norris, M. A. Pessot, and G. A. Mourou, Time-Resolved Observation of Electron-Phonon Relaxation in Copper, *Phys. Rev. Lett.* **58**, 1212 (1987).
- [45] J. Simoni and J. Daligault, First-Principles Determination of Electron-Ion Couplings in the Warm Dense Matter Regime, *Phys. Rev. Lett.* **122**, 205001 (2019).
- [46] N. Jourdain, L. Lecherbourg, V. Recoules, P. Renaudin, and F. Dorchies, Electron-ion thermal equilibration dynamics in femtosecond heated warm dense copper, *Phys. Rev. B* **97**, 075148 (2018).
- [47] A. Grolleau, F. Dorchies, N. Jourdain, K. Ta Phuoc, J. Gautier, B. Mahieu, P. Renaudin, V. Recoules, P. Martinez, and L. Lecherbourg, Femtosecond Resolution of the Nonballistic Electron Energy Transport in Warm Dense Copper, *Phys. Rev. Lett.* **127**, 275901 (2021).
- [48] Z. Lin, L. V. Zhigilei, and V. Celli, Electron-phonon coupling and electron heat capacity of metals under conditions of strong electron-phonon nonequilibrium, *Phys. Rev. B* **77**, 075133 (2008).
- [49] X. Y. Wang, D. M. Riffe, Y. S. Lee, and M. C. Downer, Time-resolved electron-temperature measurement in a highly excited gold target using femtosecond thermionic emission, *Phys. Rev. B* **50**, 8016 (1994).
- [50] N. A. Smirnov, Copper, gold, and platinum under femtosecond irradiation: Results of first-principles calculations, *Phys. Rev. B* **101**, 094103 (2020).
- [51] Y. Zhang *et al.*, Coherent modulation of the electron temperature and electron-phonon couplings in a 2D material, *Proc. Natl. Acad. Sci. U.S.A.* **117**, 8788 (2020).
- [52] M. Z. Mo *et al.*, Determination of the electron-lattice coupling strength of copper with ultrafast MeV electron diffraction, *Rev. Sci. Instrum.* **89**, 10C108 (2018).
- [53] M. W. C. Dharma-wardana, Nature of Coupled-Mode Contributions to Hot-Electron Relaxation in Semiconductors, *Phys. Rev. Lett.* **66**, 197 (1990).
- [54] J. Vorberger and D. O. Gericke, Coupled mode effects on energy transfer in weakly coupled, two-temperature plasmas, *Phys. Plasmas* **16**, 082702 (2009).
- [55] A. Rousse *et al.*, Non-thermal melting in semiconductors measured at femtosecond resolution, *Nature (London)* **410**, 65 (2001).
- [56] D. Von der Linde *et al.*, ‘Ultrafast’ extended to x-rays: Femtosecond time-resolved x-ray diffraction, *Z. Phys. Chem.* **215**, 1527 (2001).
- [57] T. Kampftrath, L. Perfetti, F. Schapper, C. Frischkorn, and M. Wolf, Strongly Coupled Optical Phonons in the Ultrafast Dynamics of the Electronic Energy and Current Relaxation in Graphite, *Phys. Rev. Lett.* **95**, 187403 (2005).
- [58] I. Barke *et al.*, The 3D-architecture of individual free silver nanoparticles captured by x-ray scattering, *Nat. Commun.* **6**, 6187 (2015).